

Deep learning of committor for ion dissociation and interpretable analysis of solvent effects using atom-centered symmetry functions

Kenji Okada,¹ Kazushi Okada,¹ Kei-ichi Okazaki,^{2,3,a)} Toshifumi Mori,^{4,5,b)} Kang Kim,^{1,c)} and Nobuyuki Matubayasi^{1,d)}

¹⁾*Division of Chemical Engineering, Department of Materials Engineering Science, Graduate School of Engineering Science, The University of Osaka, Toyonaka, Osaka 560-8531, Japan*

²⁾*Research Center for Computational Science, Institute for Molecular Science, Okazaki, Aichi 444-8585, Japan*

³⁾*Graduate Institute for Advanced Studies, SOKENDAI, Okazaki, Aichi 444-8585, Japan*

⁴⁾*Institute for Materials Chemistry and Engineering, Kyushu University, Kasuga, Fukuoka 816-8580, Japan*

⁵⁾*Interdisciplinary Graduate School of Engineering Sciences, Kyushu University, Kasuga, Fukuoka 816-8580, Japan*

(Dated: 11 December 2025)

The association and dissociation of ion pairs in water are fundamental to physical chemistry, yet their reaction coordinates are complex, involving not only interionic distance but also solvent-mediated hydration structures. These processes are often represented by free-energy landscapes constructed from collective variables (CVs), such as interionic distance and water bridging structures; however, it remains uncertain whether such representations reliably capture the transition pathways between the two associated and dissociated states. In this study, we employ deep learning to identify reaction coordinates for NaCl ion pair association and dissociation in water, using the committor as a quantitative measure of progress along the transition pathway through the transition state. The solvent environment surrounding the ions is encoded through descriptors based on atom-centered symmetry functions (ACSFs), which serve as input variables for the neural network. In addition, an explainable artificial intelligence technique is applied to identify ACSFs that contribute to the reaction coordinate. A comparative analysis of their correlation with CVs representing water bridging structures, such as interionic water density and the number of water molecules coordinating both ions, further provides a molecular-level interpretation of the ion association-dissociation mechanism in water.

I. INTRODUCTION

To understand transition processes involving many degrees of freedom in complex molecular systems, such as ion dissociation and isomerization, it is essential to examine the corresponding free-energy landscape.¹⁻⁴ From the system's total degrees of freedom, a collective variable (CV) X , for example, an interatomic distance, bond angle, or dihedral angle, is conventionally employed. The free-energy landscape can be described by the potential of mean force (PMF), $-k_B T \ln P(X)$, where $P(X)$ denotes the probability distribution function with respect to X . When the resulting free-energy landscape exhibits two minima separated by a saddle point, these minima correspond to distinct stable states, while the transition pathway is expected to pass in the vicinity of the saddle point. In this context, the saddle point represents the transition state (TS), and the CV X can be regarded as the reaction coordinate (RC). However, a fundamental difficulty arises in that the selection of X is arbitrary.

A method known as committor analysis is commonly used to evaluate CV as an appropriate RC.⁵⁻¹³ The committor, p_B^* , is defined as the probability that a trajectory initiated from a given configuration reaches the product state B before reaching the reactant state A. A value of $p_B^* \approx 0$ indicates that the

configuration lies near state A, whereas $p_B^* \approx 1$ signifies proximity to state B. Configurations for which $p_B^* = 0.5$ correspond to the TS ensemble. When a CV is chosen such that configurations with $p_B^* = 0.5$ coincide with the saddle point on the free-energy landscape, that CV can be regarded as the appropriate RC. However, because a large number of possible CVs exist and the evaluation is typically performed by trial and error, an automated and systematic approach is required.¹⁴

Machine learning approaches based on committor analysis have shown considerable promise for identifying RC, leading to the development of various methodological frameworks.¹⁵⁻³⁶ Recently, we developed a deep learning framework trained on committor values p_B^* of configurations sampled near the saddle point region from molecular dynamics (MD) simulations.³⁷ In this approach, candidate CVs are employed as input features, and the corresponding RC is predicted as the output variable through the neural network using p_B^* as the learning target. Because deep learning models often behave as black boxes, eXplainable AI (XAI) techniques are further employed to quantify the contribution of each input variable to the predicted RC. This approach enables the identification of CVs with significant contribution, providing a representation of the TS on the free-energy landscape that is consistent with the underlying transition pathways.

As an application, we previously investigated the isomerization reaction of alanine dipeptide and identified dihedral angles that primary contributor to the RC.³⁷ Furthermore, we demonstrated that the isomerization can be characterized not only by the dihedral angles but also by specific interatomic distances.³⁸ We also investigated how hyperparameter tuning

^{a)}Electronic mail: keokazaki@ims.ac.jp

^{b)}Electronic mail: toshi_mori@cm.kyushu-u.ac.jp

^{c)}Electronic mail: kk@cheng.es.osaka-u.ac.jp

^{d)}Electronic mail: nobuyuki@cheng.es.osaka-u.ac.jp

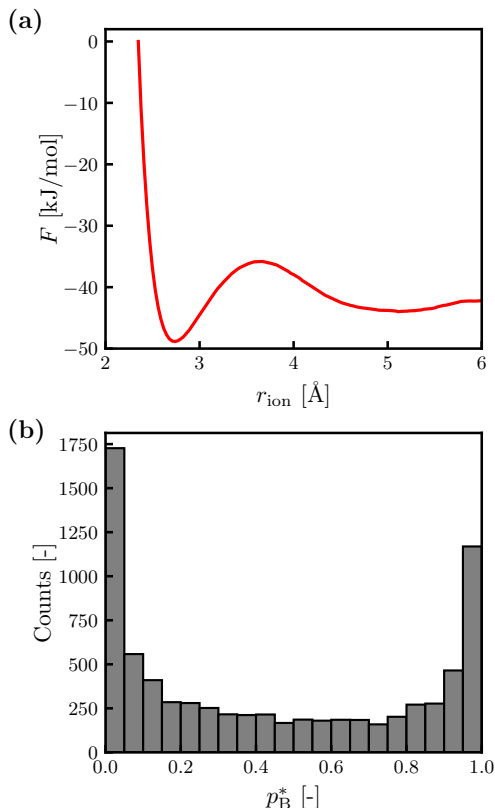


FIG. 1. (a) PMF $F(r_{\text{ion}})$ as a function of the interionic distance r_{ion} . (b) Distribution of Committor p_B^* evaluated for configurations sampled within the range $3.2 \text{ \AA} < r_{\text{ion}} < 4.3 \text{ \AA}$.

in the neural network model influences the performance and reliability of the identified RC.³⁹

In this study, we applied an explainable deep learning-based analytical framework for identifying appropriate CVs serving as RC to the association and dissociation process of NaCl ion pair in water. This process may appear to be described adequately by the interionic distance r_{ion} .^{40–46} However, r_{ion} alone does not fully capture the underlying mechanism, as previous studies have indicated that water bridging structures formed by intervening water molecules play a critical role.^{47–49} Here, particular attention is focused on the arrangement of water molecules surrounding the ion pair. Specifically, at the TS, a bridging configuration is expected to form, in which the O and H atoms of a water molecule simultaneously coordinate to the Na and Cl ions, respectively. Geissler *et al.* proposed a mechanism in which a water molecule initially coordinating the Na ion migrate toward the Cl ion side, generating space to locate new water molecules.⁴⁷ Thus, changes in the coordination number of water molecules near the ions at the TS are thought to facilitate the activation of the dissociation process.

Previous studies have further evaluated CVs that represent water bridging structures.^{50–58} In particular, CVs such as the interionic water density and the water molecules coordinating both ions were identified as important through analyses of free-energy landscapes. These studies revealed that the formation of water bridges reduces the dissociation energy barrier,

thereby facilitating the ion pair dissociation.

Because these CVs are defined based on the physical intuition and are hand-crafted, we instead employ atom-centered symmetry functions (ACSFs), widely used as descriptors in machine learning potentials,^{59–61} as non-empirical CVs. Owing to their invariance under translational and rotational operations, ACSFs provide a systematic and comprehensive representation of the solvent environment. Geiger and Dellago proposed a machine learning method using ACSFs to classify the local structures of amorphous and crystalline structures.⁶² Extended methods for identifying local structures in MD simulations, based on the neural network framework developed by Geiger and Dellago, have also been proposed.^{63,64} Furthermore, Jung *et al.* employed ACSFs to represent the solvent environment and trained committor values using machine learning combined with symbolic regression, focusing on ion pair dissociation in water.²⁸ However, while ACSFs provide a systematic and comprehensive description, they remain inherently abstract. Therefore, we aim to enhance interpretability by relating ACSFs to the hand-crafted CVs that represent water bridging structures as reference features.

II. METHODS

A. MD simulations and committor evaluation

MD simulations were performed for NaCl ion pair in water. Specifically, the system had a linear dimension of 40 \AA and was simulated under periodic boundary conditions. It comprised one pair of Na and Cl ions by the AMBER99 force field⁶⁵ and 2048 TIP/4P-Ew⁶⁶ water molecules. Initially, MD simulations using the umbrella sampling method were performed at 300 K for 10 ns with the time step of 2 fs. A harmonic bias with a spring constant of $k = 500 \text{ kJ mol}^{-1} \text{ \AA}^{-2}$ was applied at 30 window positions spaced at 0.2 \AA intervals over the interion distance range from 2.2 \AA to 8.0 \AA . The temperature was controlled using the Nosé–Hoover thermostat. The real space cut-off length was set to 12 \AA , and long range electrostatic interactions were evaluated using the particle mesh Ewald method. The potential of mean force (PMF) as a function of r_{ion} was then constructed using the WHAM method. The resulting PMF is illustrated in Fig. 1(a).

Next, an additional umbrella sampling was performed centered at $r_{\text{ion}} = 3.65 \text{ \AA}$ with a harmonic bias of a spring constant $k = 100 \text{ kJ mol}^{-1} \text{ \AA}^{-2}$. A total of 7600 configurations were extracted for interionic distances between $3.2 \text{ \AA} < r_{\text{ion}} < 4.3 \text{ \AA}$. This distance range was chosen to cover the saddle point position at $r_{\text{ion}} = 3.6 \text{ \AA}$ on the PMF, as shown in Fig. 1(a). The associated state A is defined for $r < 3.2 \text{ \AA}$, while the dissociated state B is defined for $r > 4.3 \text{ \AA}$. The committor p_B^* for each sampled configuration was evaluated by performing 100 independent 1 ps MD simulations at 300 K, each initialized with velocities randomly drawn from the Maxwell–Boltzmann distribution for the sampled configuration. The distribution of the committor p_B^* is shown in Fig. 1(b). It can be seen that p_B^* tends toward 0 and 1, without exhibiting a pronounced peak near 0.5. This result is consistent with the findings of pre-

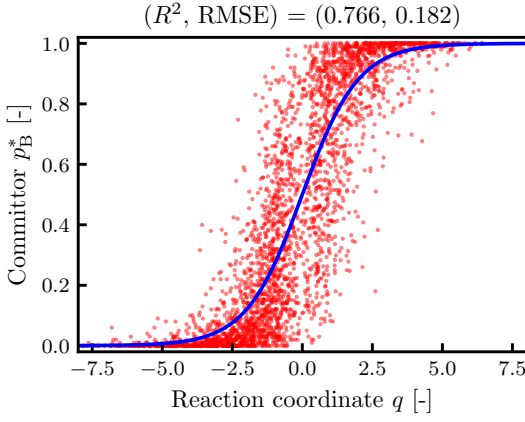


FIG. 2. Relationship between committor p_B^* and the RC q predicted by the neural network trained model using the test dataset (3040 points). The blue curve represents the sigmoidal function, $p_B(q) = (1 + \tanh(q))/2$.

vious work,⁴⁷ indicating that the CV of r_{ion} is insufficient to account for the TS. All the MD simulations were performed using GROMACS 2024.5.⁶⁷

B. Neural network learning and SHAP

The neural network used in this study consists of five hidden layers, with the odd-numbered layers containing 400 nodes and even-numbered layers containing 200 nodes. Candidate CVs serve as the input features, and the output is the variable q . The network is trained to regress the relationship between q and the committor p_B^* onto the sigmoid function $p_B(q) = (1 + \tanh(q))/2$. Consequently, q serves as the RC.

The cross-entropy between $p_B(q) = (1 + \tanh(q))$ and p_B^* was employed as the loss function, which is expressed as

$$\mathcal{H}(p_B, p_B^*) = - \sum_k p_B^*(r_k) \ln p_B(q) - \sum_k (1 - p_B^*(r_k)) \ln [1 - p_B(q)], \quad (1)$$

where r_k denotes the k -th initial configuration.^{21,68} This equation is derived from the Kullback–Leibler divergence, which quantifies the discrepancy between the distribution of the committor p_B^* and the expected committor function $p_B(q)$.⁶⁸ It is also noted that Eq. (1) represents a generalization of the log-likelihood function.¹⁷ The dataset of candidate CVs and committor p_B^* from 7600 configurations was partitioned into training, validation, and test datasets at a ratio of 5:1:4. Furthermore, overfitting was prevented using Dropout (probability 0.5) and L2 regularization (coefficient 0.001). Training was performed using the AdaMax optimizer with a batch size of 256 and a learning rate of 1×10^{-5} , over 4000 epochs.

To enhance the interpretability of the neural network model, we employed the SHapley Additive exPlanations (SHAP) method as an XAI technique.⁶⁹ This method quantifies the contribution of each input feature to the predictions, providing an interpretable model of feature importance. Specifically,

SHAP uses an additive feature attribution framework using Shapley values based on game theory, ensuring a fair and consistent distribution of prediction values among input features. This enables the non-empirical identification of CVs that effectively describe the RC.

C. Input features as candidate CVs

The ACSF describes how many atoms are located at specific distances and angles around a central atom.⁶⁰ To represent the solvent environment around the ions, we employed two types of ACSFs, G_i^2 and G_i^5 for reference atom i , as input variables for neural networks. These functions are defined as

$$G_i^{2,Z_1} = \sum_{j \neq i}^{|Z_1|} e^{-\eta(R_{ij}-R_s)^2} \cdot f_c(R_{ij}), \quad (2)$$

$$G_i^{5,Z_1,Z_2} = 2^{1-\zeta} \sum_{j \neq i}^{|Z_1|} \sum_{k \neq i}^{|Z_2|} (1 + \lambda \cos \theta_{ijk})^\zeta \cdot e^{-\eta((R_{ij}-R_s)^2 + (R_{ik}-R_s)^2)} \cdot f_c(R_{ij}) \cdot f_c(R_{ik}), \quad (3)$$

respectively. Note that R_{ij} (R_{ik}) represents the distance between atoms i and j (k), and θ_{ijk} denotes the angle formed by atoms j and k with atom i at the center. Z_1 and Z_2 represent atomic species surrounding the reference atom and the absolute value notation denotes their respective atomic numbers. Furthermore, the cut-off function is introduced as

$$f_c(R_{ij}) = \begin{cases} 0.5 \cdot [\cos(\pi R_{ij}/R_c) + 1] & \text{for } R_{ij} < R_c \\ 0 & \text{for } R_{ij} > R_c, \end{cases} \quad (4)$$

with the cut-off radius, R_c .

The ACSF G_i^2 is defined as the sum of a Gaussian function weighted by the cutoff function. The width of the Gaussian is determined by the parameter η , while its center can be positioned at a specific radial distance using the parameter R_s . This function is particularly suitable for characterizing the spherical shell environment surrounding a reference atom. The ACSF G_i^5 extends G_i^2 by incorporating an additional target atom and including an angular component. The parameter λ can take values of 1 or -1 , shifting the maximum of the cosine function to $\theta_{ijk} = 0^\circ$ and $\theta_{ijk} = 180^\circ$, respectively. The parameter ζ controls the angular resolution, with larger values of ζ corresponding to a narrower range of nonzero contributions in the ACSF.

In this study, we used $R_c = 10.0 \text{ \AA}$, $\eta = 2.0 \text{ \AA}^{-2}$ for G^2 , and $\eta = 1.2 \text{ \AA}^{-2}$ for G^5 . Regarding atomic combinations, four types were used for G^2 : (i - Z_1) = (Na-O), (Na-H), (Cl-O), (Cl-H). For G^5 , (Z_1 - i - Z_2) = (O-Na-O), (O-Na-H), (H-Na-H), (Cl-Na-H), (Cl-Na-O), (O-Cl-O), (O-Cl-H), (H-Cl-H), (Na-Cl-H), (Na-Cl-O). By systematically varying other parameters, R_s , λ , and ζ , we generated a total of 1296 descriptors, comprising 36 G^2 and 1260 G^5 . Detailed definitions of the input features of two ACSFs, G^2 and G^5 , are provided in Tables S1 of the Supplementary Material. All input variables for the neural network were standardized.

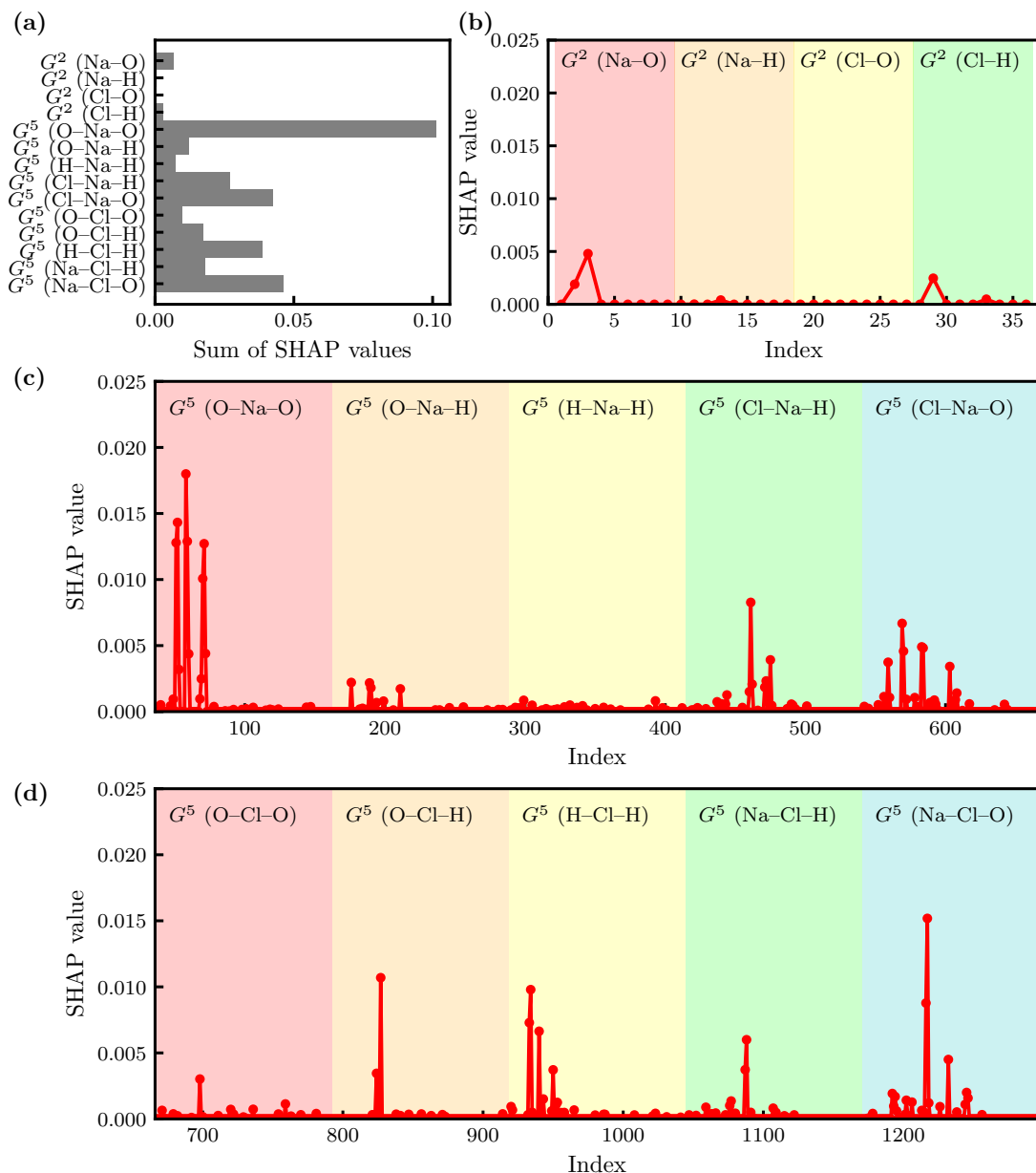


FIG. 3. Feature contribution of each CV evaluated by the absolute SHAP value. (a): Summed SHAP values for each atom combination (i - Z_1) in G^2 and (Z_1 - i - Z_2) in G^5 descriptors. (b): Index dependence of SHAP values for G^2 descriptors. (c) and (d): Index dependence of SHAP values for G^5 descriptors.

III. RESULTS AND DISCUSSION

A. Predicted RC

We first present the result of the neural network training on the committor p_B^* . Figure 2 shows the relationship between p_B^* and q using the test data. The model performance was evaluated using two metrics: the coefficient of determination R^2 and the root-mean-square error (RMSE), which were found to be $(R^2, \text{RMSE}) = (0.766, 0.128)$. Our previous study investigated the isomerization of alanine dipeptides using the same neural network architecture; however, the present model ex-

hibited slightly reduced predictive performance relative to the earlier one.³⁸ This decrease is likely attributable to the substantial increase in degrees of freedom arising from the inclusion of solvent, although we consider the training to have been sufficiently converged.

B. Feature contribution of CV by SHAP

The feature contribution of each input CV to the RC predicted by the neural network was evaluated using SHAP. The average of 100 SHAP values randomly sampled from the test

TABLE I. Top five dominant indices, those parameters, and absolute SHAP values among G^5 (O-Na-O) descriptors.

index	R_s [Å]	λ	ζ	absolute SHAP value
58	2.0	-1	1	0.0180
52	2.0	1	2	0.0143
59	2.0	-1	2	0.0129
51	2.0	1	1	0.0128
71	3.0	1	32	0.0127

TABLE II. Top five dominant indices, those parameters, and absolute SHAP values among G^5 (Na-Cl-O) descriptors.

index	R_s [Å]	λ	ζ	absolute SHAP value
1217	4.0	1	16	0.0152
1216	4.0	1	8	0.0088
1232	5.0	1	32	0.0045
1245	6.0	1	16	0.0020
1192	2.0	-1	1	0.0019

dataset of 3040 configurations was calculated and the results are plotted in Fig. 3.

Figure 3(a) shows the summed SHAP values for each atomic combination in the G^2 and G^5 descriptors. Overall, the contribution of G^2 is minimal, indicating that the information encoded in G^2 is effectively subsumed by the G^5 descriptors. Notably, within G^5 , $(Z_1-i-Z_2)=(\text{O}-\text{Na}-\text{O})$ descriptors exhibited the largest contribution, followed by $(\text{Na}-\text{Cl}-\text{O})$, $(\text{Cl}-\text{Na}-\text{O})$, and $(\text{H}-\text{Cl}-\text{H})$. This result indicates that the coordination of water O atoms around the Na, as well as configurations involving one ion and a water O atom relative to the other ion, play a central role. In comparison, the contribution of water H atoms around Cl ion is minor.

Table I lists the top five contributors the within G^5 (O-Na-O) descriptors along with their corresponding absolute SHAP values. The G^5 descriptor at index 58 (denoted as G_{58}^5), corresponding to $(\text{O}-\text{Na}-\text{O})$ with the highest contribution, has the distance and angular sensitivities of $R_s = 2.0$ Å, $\lambda = -1$, and $\zeta = 1$. This indicates that water O atoms within a spherical shell of radius $R_s = 2.0$ Å around Na make a significant contribution. Note that $R_s = 2.0$ Å approximately corresponds to the Lennard-Jones diameter of Na. In contrast, the low angular resolution ($\zeta = 1$) suggests that angular dependence is not particularly important for characterizing the distribution of O atoms around Na. Typical structures are schematically illustrated in Fig. 4(a). The other descriptors listed in Table I exhibit similar properties, while their parameter values differ slightly.

Within the G^5 (Na-Cl-O) descriptors, listed in Table II, index 1217 (denoted as G_{1217}^5) contributes the most significantly, characterized by $R_s = 4.0$ Å, $\lambda = 1$, and $\zeta = 16$. At this high angular sensitivity ($\zeta = 16$), the angular component $2^{1-\zeta}(1 + \cos \theta_{ijk})^\zeta$ decreases from unity and approaches zero near $\theta_{ijk} \approx 60^\circ$, indicating that the dominant Na-Cl-O bond angles lie within this range. This implies that water O atoms located in the overlapping region of the hydration shells, cor-

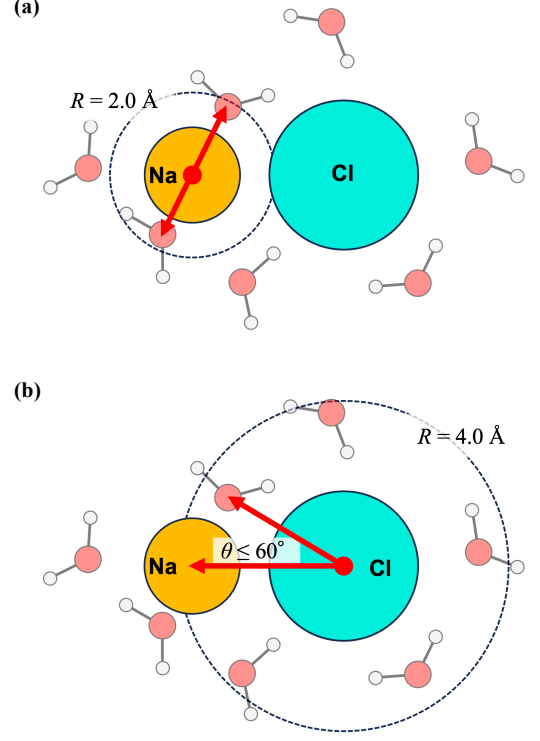


FIG. 4. Schematic illustration of water O atoms within 2 Å of Na (a) and water O atoms within the 4 Å hydration shell of Cl (b), characterized by two ACSF descriptors, G_{58}^5 and G_{1217}^5 , respectively.

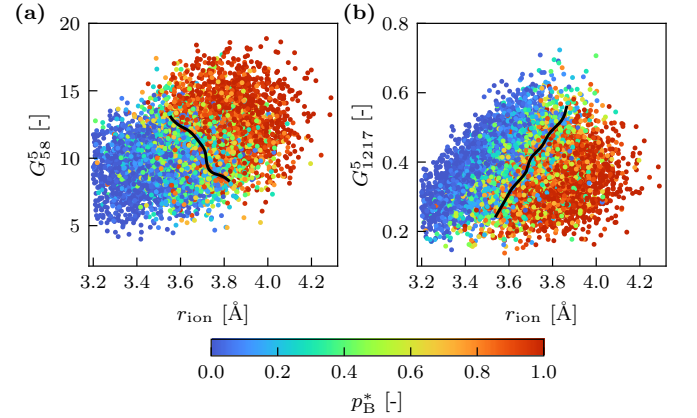


FIG. 5. Distribution of committor p_B^* dataset in the two-dimensional surface using the interionic distance r_{ion} and G_{58}^5 (a) and G_{1217}^5 (b). Committor values are colored according to the bottom color bar. The black lines are drawn as follows. The ranges of the x- and y-axis values were each divided into 200 grid points (forming a 200×200 grid), and the average committor value p_B^* within each grid cell was computed. After applying cubic interpolation for smoothing, contour lines corresponding to $p_B^* = 0.5$ were plotted.

responding to $R_s = 4$ Å separation between Na and Cl ions, slightly larger than the saddle point distance $r_{\text{ion}} = 3.6$ Å of the PMF, are key contributors [see the schematic illustration in Fig. 4(b)]. The other descriptors listed in Table II also imply similar structural features, except for index 1192.

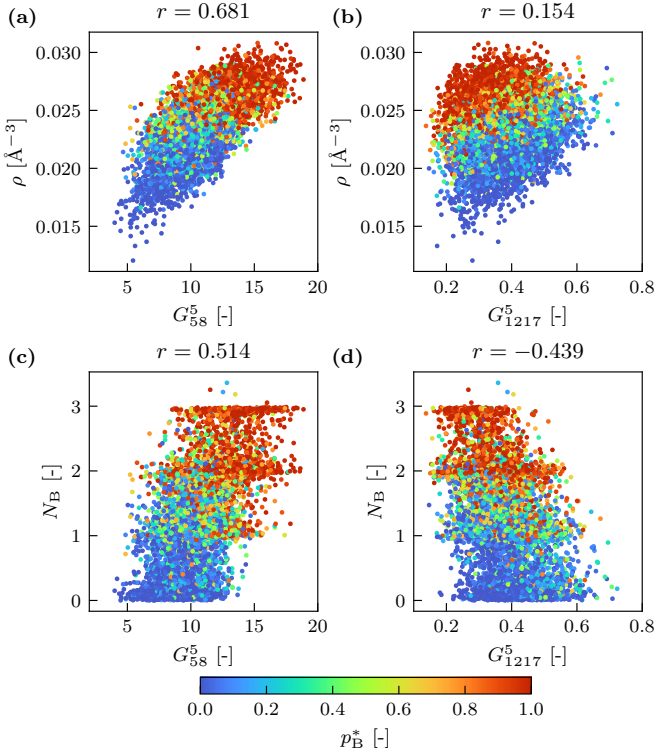


FIG. 6. Distribution of committor p_B^* dataset in the two-dimensional surface using the combinations (G_{58}^5, ρ) (a), (G_{1217}^5, ρ) (b), (G_{58}^5, N_B) (c), and (G_{1217}^5, N_B) (d). Committor values are colored according to the bottom color bar. The r -value represents the correlation coefficient for each panel.

It is here important to characterize the p_B^* dataset using the interionic distance, r_{ion} , in combination with either of the two ACSF descriptors, G_{58}^5 or G_{1217}^5 , as shown in Fig. 5. Figure 5 shows that the distribution of the committor p_B^* transitions continuously from the associated state ($p_B^* \approx 0$) to the dissociated state ($p_B^* \approx 1$), with the transition state ($p_B^* = 0.5$) forming a clear separatrix line. Figure 5(a) shows that when the interionic distance is fixed at the saddle point ($r_{\text{ion}} = 3.6$ Å) of the PMF shown in Fig. 1(a), the committor value increases with increasing G_{58}^5 , indicating that O atoms surrounding Na are critical for the ion pair dissociation. Conversely, Fig. 5(b) demonstrates that as G_{1217}^5 decreases, the committor value increases, suggesting that ion pair dissociation requires a reduction in the density of O atoms belonging simultaneously to the hydration shells of both Na and Cl. Therefore, the two ACSF descriptors, G_{58}^5 and G_{1217}^5 , identified through the neural network and SHAP analysis, highlight the importance of water bridging structures in the association and dissociation process of NaCl ion pair in water, consistent with physical intuition.

C. Comparative analysis with CVs representing water bridging structure

The ACSF descriptors, G_{58}^5 and G_{1217}^5 , is expected to effectively capture the structural feature corresponding to wa-

ter molecules bridging the two ions. Finally, it is important to examine the correlations of G_{58}^5 and G_{1217}^5 with hand-crafted CVs that represent water bridging structures. Müllen *et al.* calculated a total of 71 CVs representing water bridging structures.⁵⁰ Then, the combinations of up to three CVs were employed in the Inertial Likelihood Maximization method.⁷⁰ Among these, the interionic water density ρ and the number of bridging waters N_B were found to contribute most significantly to the RC. Specifically, the interionic water density ρ is defined by

$$\rho = \left(\frac{1}{2\pi\sigma^2} \right)^{3/2} \sum_w \exp \left(-\frac{|\mathbf{r}_w - \mathbf{r}_{\text{mid}}|^2}{2\sigma^2} \right), \quad (5)$$

where \mathbf{r}_w and \mathbf{r}_{mid} represent the center-of-mass position of the w -th water molecule and the midpoint between Na and Cl ions, respectively. The parameter σ controls the number of water molecules within the volume $(2\pi\sigma^2)^{3/2}$, which is chosen as $r_{\text{ion}}/2$. The number of bridging waters N_B is calculated based on the following two steps: The ion coordination function is defined as

$$f_{s-w} = \frac{1 - \tanh[a(R_{s-w} - b)]}{2}, \quad (6)$$

where the subscript s represents an ion species, *i.e.*, Na or Cl. The distance R_{s-w} corresponds to the w -th water O atom when calculating Na coordination, and to the w -th water H atom when calculating Cl coordination. The parameters a and b are set to 3 Å^{-1} and 3.2 Å , respectively. The number of waters coordinating to both ions simultaneously is then

$$N_B = \sum_w \min(f_{\text{Na}^+-w}, f_{\text{Cl}^--w}). \quad (7)$$

Figure 6 shows the distribution of the committor p_B^* dataset on the two-dimensional surfaces using the combinations (G_{58}^5, ρ) (a), (G_{1217}^5, ρ) (b), (G_{58}^5, N_B) (c), and (G_{1217}^5, N_B) (d). For each combination of variables, the corresponding correlation coefficient r was calculated and is presented in Fig. 6. The interionic water density ρ shows a positive correlation with G_{58}^5 and a weak negative correlation with G_{1217}^5 . Similarly, the number of bridging water molecules N_B exhibits a positive correlation with G_{58}^5 , while its correlation with G_{1217}^5 is slightly stronger than that of ρ . In other words, increases in ρ and N_B , which correlate positively with G_{58}^5 and negatively with G_{1217}^5 , promotes dissociation from the associated state, consistent with the separatrix lines described in Fig. 5. Furthermore, the distributions of the committor p_B^* in each panel of Fig. 6 show a clear separation between the associated and dissociated states. In summary, the hand-crafted CVs, ρ and N_B , are validated as meaningful contributors to the RC through the identified two ACSF descriptors, G_{58}^5 and G_{1217}^5 .

IV. CONCLUSIONS

In this study, we identified the RC for the NaCl ion dissociation–association process using deep learning with the committor p_B^* as the training target. The committor p_B^* values were

obtained by initial configurations obtained via umbrella sampling constrained along the interionic distance r_{ion} , followed by 1 ps MD trajectories. To describe the solvent environment around the ions, we introduced ACSFs, G^2 and G^5 , as CVs and used as input variables to the neural network. The model was trained by minimizing the cross entropy so that the relationship between p_B^* and the RC q followed the sigmoidal function, $p_B(q) = (1 + \tanh(q))/2$.

To interpret the resulting RC q , we applied SHAP, an XAI technique. This analysis revealed that the ACSF descriptors, G_{58}^5 and G_{1217}^5 , characterizing the O atom environment around Na ion and the O atoms within the hydration shell of Na and Cl ions, respectively make dominant contributions to the RC. Jung *et al.* demonstrated the importance of ACSFs describing the water O atoms around cations, a finding consistent with our G_{58}^5 .²⁸ Additionally, we clarified that G_{1217}^5 , characterizing the O atoms within the hydration shells of Na and Cl, also makes a dominant contribution. We further demonstrated that these two ACSF descriptors effectively capture the water bridging structure essential to ion dissociation, as evidenced by their correlations with conventionally defined CVs such as the interionic water density ρ and number of bridging water molecules N_B .⁵⁰

The RC obtained through our integrated approach, which combines committor based deep learning, ACSF descriptors, and XAI, provides a refined molecular picture of solvent effects. Moreover, this methodology offers a general strategy applicable to a wide range of condensed phase reactions in which solvent reorganization plays a crucial role. It can be extended to processes such as ligand binding, nucleation, and biomolecular conformational changes, where the solvent environment significantly influence the TS.

SUPPLEMENTARY MATERIAL

The supplementary material includes definitions of input variables and those ACSF parameters, reference atom i , Z_1 , Z_2 , R_s , λ , and ζ (Tables S1) in the CSV format.

ACKNOWLEDGMENTS

The authors acknowledge Professors Yasutaka Kitagawa and Ryohei Kishi for valuable comments. This work was supported by JSPS KAKENHI Grant-in-Aid Grant Nos. JP23K23858, JP25H02299, JP23K23303, JP23KK0254, JP24K21756, JP25H02464, JP25K02235, JP25K00968, JP24H01719, JP22K03550, and JP23H02622. We acknowledge support from the Fugaku Supercomputing Project (Nos. JPMXP1020230325 and JPMXP1020230327) and the Data-Driven Material Research Project (No. JPMXP1122714694) from the Ministry of Education, Culture, Sports, Science, and Technology and by Maruho Collaborative Project for Theoretical Pharmaceuticals. The numerical calculations were performed at Research Center of Computational Science, Okazaki Research Facilities, National Institutes of Natural Sciences (Projects:

25-IMS-C052, 25-IMS-C105, 25-IMS-C227).

AUTHOR DECLARATIONS

CONFLICT OF INTEREST

The authors have no conflicts to disclose.

DATA AVAILABILITY STATEMENT

The data that support the findings of this study are available from the corresponding author upon reasonable request.

- ¹C. Chipot, A. Pohorille, A. W. Castleman, J. P. Toennies, K. Yamanouchi, and W. Zinth, eds., *Free Energy Calculations: Theory and Applications in Chemistry and Biology* (Springer, Berlin, Heidelberg, 2007).
- ²D. M. Zuckerman, *Statistical Physics of Biomolecules: An Introduction* (CRC Press, Boca Raton, FL, 2010).
- ³B. Peters, *Reaction Rate Theory and Rare Events* (Elsevier, Amsterdam, 2017).
- ⁴F. Pietrucci, "Strategies for the exploration of free energy landscapes: Unity in diversity and challenges ahead," *Rev. Phys.* **2**, 32–45 (2017).
- ⁵V. S. Pande, A. Y. Grosberg, T. Tanaka, and D. S. Rokhsar, "Pathways for protein folding: Is a new view needed?" *Curr. Opin. Struct. Biol.* **8**, 68–79 (1998).
- ⁶P. G. Bolhuis, C. Dellago, and D. Chandler, "Reaction coordinates of biomolecular isomerization," *Proc. Natl. Acad. Sci. U.S.A.* **97**, 5877–5882 (2000).
- ⁷P. G. Bolhuis, D. Chandler, C. Dellago, and P. L. Geissler, "TRANSITION PATH SAMPLING: Throwing Ropes Over Rough Mountain Passes, in the Dark," *Annu. Rev. Phys. Chem.* **53**, 291–318 (2002).
- ⁸G. Hummer, "From transition paths to transition states and rate coefficients," *J. Chem. Phys.* **120**, 516–523 (2004).
- ⁹R. B. Best and G. Hummer, "Reaction coordinates and rates from transition paths," *Proc. Natl. Acad. Sci. U.S.A.* **102**, 6732–6737 (2005).
- ¹⁰W. E, W. Ren, and E. Vanden-Eijnden, "Transition pathways in complex systems: Reaction coordinates, isocommittor surfaces, and transition tubes," *Chem. Phys. Lett.* **413**, 242–247 (2005).
- ¹¹H. Jung, K.-i. Okazaki, and G. Hummer, "Transition path sampling of rare events by shooting from the top," *J. Chem. Phys.* **147**, 152716 (2017).
- ¹²J. Rogal, "Reaction coordinates in complex systems-a perspective," *Eur. Phys. J. B* **94**, 223 (2021).
- ¹³P. G. Bolhuis and D. W. H. Swenson, "Transition Path Sampling as Markov Chain Monte Carlo of Trajectories: Recent Algorithms, Software, Applications, and Future Outlook," *Adv. Theory Simul.* **4**, 2000237 (2021).
- ¹⁴W. Li and A. Ma, "Recent Developments in Methods for Identifying Reaction Coordinates," *Mol. Simul.* **40**, 784–793 (2014).
- ¹⁵A. Ma and A. R. Dinner, "Automatic Method for Identifying Reaction Coordinates in Complex Systems," *J. Phys. Chem. B* **109**, 6769–6779 (2005).
- ¹⁶B. Peters and B. L. Trout, "Obtaining reaction coordinates by likelihood maximization," *J. Chem. Phys.* **125**, 054108 (2006).
- ¹⁷B. Peters, G. T. Beckham, and B. L. Trout, "Extensions to the likelihood maximization approach for finding reaction coordinates," *J. Chem. Phys.* **127**, 034109 (2007).
- ¹⁸B. Peters, "Reaction Coordinates and Mechanistic Hypothesis Tests," *Annu. Rev. Phys. Chem.* **67**, 669–690 (2016).
- ¹⁹E. Schneider, L. Dai, R. Q. Topper, C. Drechsel-Grau, and M. E. Tuckerman, "Stochastic Neural Network Approach for Learning High-Dimensional Free Energy Surfaces," *Phys. Rev. Lett.* **119**, 150601 (2017).
- ²⁰J. Rogal, E. Schneider, and M. E. Tuckerman, "Neural-Network-Based Path Collective Variables for Enhanced Sampling of Phase Transformations," *Phys. Rev. Lett.* **123**, 245701 (2019).
- ²¹Y. Mori, K.-i. Okazaki, T. Mori, K. Kim, and N. Matubayasi, "Learning reaction coordinates via cross-entropy minimization: Application to alanine dipeptide," *J. Chem. Phys.* **153**, 054115 (2020).

- ²²L. Bonati, V. Rizzi, and M. Parrinello, "Data-Driven Collective Variables for Enhanced Sampling," *J. Phys. Chem. Lett.* **11**, 2998–3004 (2020).
- ²³L. Bonati, G. Piccini, and M. Parrinello, "Deep learning the slow modes for rare events sampling," *Proc. Natl. Acad. Sci. U.S.A.* **118**, e2113533118 (2021), arXiv:2107.03943.
- ²⁴M. Frassek, A. Arjun, and P. G. Bolhuis, "An extended autoencoder model for reaction coordinate discovery in rare event molecular dynamics datasets," *J. Chem. Phys.* **155**, 064103 (2021).
- ²⁵T. Magrino, L. Huet, A. M. Saitta, and F. Pietrucci, "Critical Assessment of Data-Driven versus Heuristic Reaction Coordinates in Solution Chemistry," *J. Phys. Chem. A* **126**, 8887–8900 (2022).
- ²⁶J. Neumann and N. Schwierz, "Artificial Intelligence Resolves Kinetic Pathways of Magnesium Binding to RNA," *J. Chem. Theory Comput.* **18**, 1202–1212 (2022).
- ²⁷G. Lazzeri, H. Jung, P. G. Bolhuis, and R. Covino, "Molecular Free Energies, Rates, and Mechanisms from Data-Efficient Path Sampling Simulations," *J. Chem. Theory Comput.* **19**, 9060–9076 (2023).
- ²⁸H. Jung, R. Covino, A. Arjun, C. Leitold, C. Dellago, P. G. Bolhuis, and G. Hummer, "Machine-guided path sampling to discover mechanisms of molecular self-organization," *Nat. Comput. Sci.* **3**, 334–345 (2023).
- ²⁹H. Chen, B. Roux, and C. Chipot, "Discovering Reaction Pathways, Slow Variables, and Commitor Probabilities with Machine Learning," *J. Chem. Theory Comput.* **19**, 4414–4426 (2023).
- ³⁰N. Naleem, C. R. A. Abreu, K. Warmuz, M. Tong, S. Kirmizialtin, and M. E. Tuckerman, "An exploration of machine learning models for the determination of reaction coordinates associated with conformational transitions," *J. Chem. Phys.* **159**, 034102 (2023).
- ³¹A. France-Lanord, H. Vroylandt, M. Salanne, B. Rotenberg, A. M. Saitta, and F. Pietrucci, "Data-Driven Path Collective Variables," *J. Chem. Theory Comput.* **20**, 3069–3084 (2024).
- ³²J. Zhang, L. Bonati, E. Trizio, O. Zhang, Y. Kang, T. Hou, and M. Parrinello, "Descriptor-Free Collective Variables from Geometric Graph Neural Networks," *J. Chem. Theory Comput.* **20**, 10787–10797 (2024).
- ³³N. S. M. Herringer, S. Dasetty, D. Gandhi, J. Lee, and A. L. Ferguson, "Permutationally Invariant Networks for Enhanced Sampling (PINES): Discovery of Multimolecular and Solvent-Inclusive Collective Variables," *J. Chem. Theory Comput.* **20**, 178–198 (2024).
- ³⁴K. Zhu, E. Trizio, J. Zhang, R. Hu, L. Jiang, T. Hou, and L. Bonati, "Enhanced Sampling in the Age of Machine Learning: Algorithms and Applications," *Chem. Rev.*, acs.chemrev.5c00700 (2025).
- ³⁵A. Megías, S. Contreras Arredondo, C. G. Chen, C. Tang, B. Roux, and C. Chipot, "Iterative variational learning of committor-consistent transition pathways using artificial neural networks," *Nat. Comput. Sci.* **5**, 592–602 (2025).
- ³⁶F. M. Dietrich and M. Salvalaglio, "On the reproducibility of free energy surfaces in machine-learned collective variable spaces," *J. Chem. Phys.* **163**, 141102 (2025).
- ³⁷T. Kikutsuji, Y. Mori, K.-i. Okazaki, T. Mori, K. Kim, and N. Matubayasi, "Explaining reaction coordinates of alanine dipeptide isomerization obtained from deep neural networks using Explainable Artificial Intelligence (XAI)," *J. Chem. Phys.* **156**, 154108 (2022).
- ³⁸K. Okada, T. Kikutsuji, K.-i. Okazaki, T. Mori, K. Kim, and N. Matubayasi, "Unveiling interatomic distances influencing the reaction coordinates in alanine dipeptide isomerization: An explainable deep learning approach," *J. Chem. Phys.* **160**, 174110 (2024).
- ³⁹K. Kawashima, T. Sato, K.-i. Okazaki, K. Kim, N. Matubayasi, and T. Mori, "Investigating the hyperparameter space of deep neural network models for reaction coordinates," *APL Mach. Learn.* **3**, 016113 (2025).
- ⁴⁰O. A. Karim and J. Andrew. McCammon, "Dynamics of a sodium chloride ion pair in water," *J. Am. Chem. Soc.* **108**, 1762–1766 (1986).
- ⁴¹O. A. Karim and J. A. McCammon, "Rate constants for ion pair formation and dissociation in water," *Chem. Phys. Lett.* **132**, 219–224 (1986).
- ⁴²G. Ciccotti, M. Ferrario, J. T. Hynes, and R. Kapral, "Constrained molecular dynamics and the mean potential for an ion pair in a polar solvent," *Chem. Phys.* **129**, 241–251 (1989).
- ⁴³G. Ciccotti, M. Ferrario, J. T. Hynes, and R. Kapral, "Dynamics of ion pair interconversion in a polar solvent," *J. Chem. Phys.* **93**, 7137–7147 (1990).
- ⁴⁴E. Guàrdia, R. Rey, and J. A. Padró, "Potential of mean force by constrained molecular dynamics: A sodium chloride ion-pair in water," *Chem. Phys.* **155**, 187–195 (1991).
- ⁴⁵R. Rey and E. Guardia, "Dynamical aspects of the sodium(1+)-chloride ion pair association in water," *J. Phys. Chem.* **96**, 4712–4718 (1992).
- ⁴⁶D. E. Smith and L. X. Dang, "Computer simulations of NaCl association in polarizable water," *J. Chem. Phys.* **100**, 3757–3766 (1994).
- ⁴⁷P. L. Geissler, C. Dellago, and D. Chandler, "Kinetic Pathways of Ion Pair Dissociation in Water," *J. Phys. Chem. B* **103**, 3706–3710 (1999).
- ⁴⁸A. J. Ballard and C. Dellago, "Toward the Mechanism of Ionic Dissociation in Water," *J. Phys. Chem. B* **116**, 13490–13497 (2012).
- ⁴⁹F. N. Brünig, J. O. Daldrop, and R. R. Netz, "Pair-Reaction Dynamics in Water: Competition of Memory, Potential Shape, and Inertial Effects," *J. Phys. Chem. B* **126**, 10295–10304 (2022).
- ⁵⁰R. G. Mullen, J.-E. Shea, and B. Peters, "Transmission Coefficients, Committors, and Solvent Coordinates in Ion-Pair Dissociation," *J. Chem. Theory Comput.* **10**, 659–667 (2014).
- ⁵¹Y. Yonetani, "Distinct dissociation kinetics between ion pairs: Solvent-coordinate free-energy landscape analysis," *J. Chem. Phys.* **143**, 044506 (2015).
- ⁵²Y. Yonetani, "Solvent-coordinate free-energy landscape view of water-mediated ion-pair dissociation," *Mol. Phys.* **115**, 2987–2998 (2017).
- ⁵³M. Salanne, S. Tazi, R. Vuilleumier, and B. Rotenberg, "Ca²⁺-Cl⁻ Association in Water Revisited: The Role of Cation Hydration," *ChemPhysChem* **18**, 2807–2811 (2017).
- ⁵⁴M. N. Joswiak, M. F. Doherty, and B. Peters, "Ion dissolution mechanism and kinetics at kink sites on NaCl surfaces," *Proc. Natl. Acad. Sci. U.S.A.* **115**, 656–661 (2018).
- ⁵⁵M. I. Oh, M. Gupta, and D. F. Weaver, "Understanding Water Structure in an Ion-Pair Solvation Shell in the Vicinity of a Water/Membrane Interface," *J. Phys. Chem. B* **123**, 3945–3954 (2019).
- ⁵⁶C. Zhang, F. Giberti, E. Sevgen, J. J. de Pablo, F. Gygi, and G. Galli, "Dissociation of salts in water under pressure," *Nat. Commun.* **11**, 3037 (2020).
- ⁵⁷D. Wang, R. Zhao, J. D. Weeks, and P. Tiwary, "Influence of Long-Range Forces on the Transition States and Dynamics of NaCl Ion-Pair Dissociation in Water," *J. Phys. Chem. B* **126**, 545–551 (2022).
- ⁵⁸K. Wilke, S. Tao, S. Calero, A. Lervik, and T. S. van Erp, "NaCl Dissociation Explored Through Predictive Power Path Sampling Analysis," *J. Chem. Theory Comput.* **21**, 4604–4614 (2025).
- ⁵⁹J. Behler and M. Parrinello, "Generalized Neural-Network Representation of High-Dimensional Potential-Energy Surfaces," *Phys. Rev. Lett.* **98**, 146401 (2007).
- ⁶⁰J. Behler, "Atom-centered symmetry functions for constructing high-dimensional neural network potentials," *J. Chem. Phys.* **134**, 074106 (2011).
- ⁶¹J. Behler, "Perspective: Machine learning potentials for atomistic simulations," *J. Chem. Phys.* **145**, 170901 (2016).
- ⁶²P. Geiger and C. Dellago, "Neural networks for local structure detection in polymorphic systems," *J. Chem. Phys.* **139**, 164105 (2013).
- ⁶³R. S. DeFever, C. Targonski, S. W. Hall, M. C. Smith, and S. Sarupria, "A generalized deep learning approach for local structure identification in molecular simulations," *Chem. Sci.* **10**, 7503–7515 (2019).
- ⁶⁴M. Fulford, M. Salvalaglio, and C. Molteni, "DeepIce: A Deep Neural Network Approach To Identify Ice and Water Molecules," *J. Chem. Inf. Model.* **59**, 2141–2149 (2019).
- ⁶⁵J. Wang, P. Cieplak, and P. A. Kollman, "How well does a restrained electrostatic potential (RESP) model perform in calculating conformational energies of organic and biological molecules?" *J. Comput. Chem.* **21**, 1049–1074 (2000).
- ⁶⁶H. W. Horn, W. C. Swope, J. W. Pitera, J. D. Madura, T. J. Dick, G. L. Hura, and T. Head-Gordon, "Development of an improved four-site water model for biomolecular simulations: TIP4P-Ew," *J. Chem. Phys.* **120**, 9665–9678 (2004).
- ⁶⁷M. J. Abraham, T. Murtola, R. Schulz, S. Páll, J. C. Smith, B. Hess, and E. Lindahl, "GROMACS: High performance molecular simulations through multi-level parallelism from laptops to supercomputers," *SoftwareX* **1**, 19–25 (2015).
- ⁶⁸T. Mori and S. Saito, "Dissecting the Dynamics during Enzyme Catalysis: A Case Study of Pin1 Peptidyl-Prolyl Isomerase," *J. Chem. Theory Comput.* **16**, 3396–3407 (2020).
- ⁶⁹S. M. Lundberg and S.-I. Lee, "A unified approach to interpreting model predictions," in *Proceedings of the 31st international conference on neural information processing systems* (Curran Associates Inc., Red Hook, NY,

2017) pp. 4768–4777.

⁷⁰B. Peters, “Inertial likelihood maximization for reaction coordinates with high transmission coefficients,” *Chem. Phys. Lett.* **554**, 248–253 (2012).